

Propagation of weak shocks in cool-core galaxy clusters in two-temperature magnetohydrodynamics with anisotropic thermal conduction

S. Komarov^{1*}, C. Reynolds¹ and E. Churazov^{2,3}

¹*Institute of Astronomy, University of Cambridge, Madingley Road, Cambridge CB3 0HA, United Kingdom*

²*Max Planck Institute for Astrophysics, Karl-Schwarzschild-Strasse 1, 85741 Garching, Germany*

³*Space Research Institute (IKI), Profsovnaya 84/32, Moscow 117997, Russia*

6 July 2020

ABSTRACT

We investigate how different magnetohydrodynamic models of propagation of a weak (Mach number ~ 1.2) shock in the core of a galaxy cluster affect its observational appearance, using the Perseus cluster as our fiducial model. In particular, we study how thermal conduction, both isotropic and anisotropic, and ion-electron temperature equilibration modify a weak shock. Strong thermal conduction is expected to produce an electron temperature precursor. Less prominent pressure and density precursors are formed as well. A longer equilibration time largely reduces the density precursor, but does not change the electron temperature precursor much. When thermal conduction becomes anisotropic, the intracluster magnetic field imprints its characteristic spatial scale on the distortions of the shock induced by heat fluxes.

Key words: galaxy clusters, thermal conduction, shocks

1 INTRODUCTION

Active galactic nuclei (AGN) in the cool cores of galaxy clusters inject an enormous amount of energy into the intracluster medium (ICM) by launching powerful relativistic jets. This process is often thought to maintain the thermodynamic stability of cluster cores by offsetting radiative cooling of the dense plasma (e.g., Churazov et al. 2000; Ruszkowski et al. 2004; Fabian et al. 2005; Zhuravleva et al. 2016; for reviews, see Fabian 2012; Werner et al. 2019). AGN jets produce a variety of physical structures: they inflate bubbles of relativistic plasma that rise in the cluster atmosphere potentially driving turbulence, launch weak shocks and sound waves, as well as inject cosmic rays into the ICM. Whether one of these processes dominates the heating of cool cores has been a matter of active debate for two decades (see Churazov et al. 2000; Reynolds et al. 2002; Dennis & Chandran 2005; Zhuravleva et al. 2014, 2016; Forman et al. 2017 for turbulent heating; Ruszkowski et al. 2004; Fabian et al. 2005; Fujita & Suzuki 2005; Shabala & Alexander 2009; Sternberg & Soker 2009; Fabian et al. 2017 for heating by sound waves; for cosmic-ray heating, see, e.g., Guo & Oh 2008). In the second scenario, sound waves propagate through the cores and gradually dissipate their energy via

thermal conduction. The efficiency of thermal conduction sets whether sound waves are able to deploy the energy over a significant fraction of the core volume before they decay. While magnetic fields in the ICM have typical magnitudes 1–10 μG (e.g., Feretti et al. 2012), they force the plasma particles to spiral around magnetic field lines with microscopic Larmor radii, so that particle diffusion across field lines is almost fully inhibited, and only parallel transport is allowed. The accumulating observational evidence based on analyzing temperature variations and radial profiles in galaxy clusters indicates that thermal conduction in the bulk of the ICM should be suppressed by factors of up to several tens (see, e.g., Markevitch et al. 2003; Fang et al. 2018 for estimates of large-scale suppression not associated with peculiar structures in the ICM where thermal isolation by magnetic-field draping may be dominant), likely beyond simple magnetohydrodynamic estimates of suppression due to tangled magnetic fields (factors ~ 3 –5; see Narayan & Medvedev 2001). Current theoretical evidence and particle-in-cell plasma simulations provide rather modest suppression factors of parallel thermal conductivity up to ~ 10 (Komarov et al. 2016; Roberg-Clark et al. 2016, 2018; Komarov et al. 2018). While the overall suppression can already be explained by a combination of effects resulting from the micro-scale plasma kinetics (that reduces parallel conductivity) and tangled magnetic field topology (that slows down the large-scale transport of heat), the relative contri-

* E-mail: skomarov@ast.cam.ac.uk

bution of parallel suppression is mainly unclear. It is the local parallel thermal conductivity that is relevant for the dissipation of sound waves. Therefore, it is helpful to look for signatures of *parallel* suppression while studying various structures in the ICM, both in observations and simulations.

Deep *Chandra* X-ray observations of the cool cores in the Perseus cluster and in the giant elliptical galaxy M87 reveal remarkably regular spherical weak shocks (for the Perseus cluster, see Fabian et al. 2006; for M87, Forman et al. 2007). These shocks have very low Mach numbers ≈ 1.2 and, therefore, propagate almost at the speed of sound. The ion and electron Coulomb mean free paths in their vicinity are ~ 0.1 kpc, below the resolution of *Chandra*. If electron thermal conduction across very weak shocks is not suppressed by kinetic instabilities, it can appreciably reduce the sharpness of temperature and even density jumps for the parameters characteristic of the Perseus and M87 cores. In this case, thermal electrons diffuse rapidly in front of a shock, forming a temperature and, to a lesser extent, pressure and density precursors. Also, because heat is transferred strictly along magnetic field lines, their topology may be imprinted on the shock producing temperature/density inhomogeneities along the front. In modelling such effects, it is important to note that the electron-ion energy equilibration time scale is three orders of magnitude (the proton-to-electron mass ratio) longer than the time between electron collisions. This means that while the jump of the electron temperature becomes smoothed, that of the ion temperature and plasma density (electron and ion densities are the same due to plasma quasineutrality) may remain much sharper.

In this paper, we perform a number of two-temperature magnetohydrodynamics simulations of weak shocks including the effects of anisotropic thermal conduction and long electron-ion equilibration time. We use the weak shock ≈ 25 kpc north-east of the Perseus center as our fiducial model. The weak shock in M87 has similar properties, however, the *Chandra* observations of the Perseus core we use for comparison with our simulations are of much higher quality due to the higher brightness of the Perseus cluster. Hydrodynamic modelling of the Perseus weak shock with thermal conduction has been done by a number of authors (Graham et al. 2008; Tang & Churazov 2018). We attempt to expand on their work by adding magnetic fields and a finite electron-ion temperature equilibration time. The paper is organized as follows. In Section 2, we describe the physical model and numerical set-up, then in Section 3, we present results of our numerical simulations and compare them with observations of the Perseus weak shock. Section 4 discusses the validity of our assumptions and potential significance of the results for current and future X-ray observations. Finally, Section 5 summarizes our findings.

2 MODEL

2.1 Equations solved

We solve the equations of two-temperature magnetohydrodynamics joined by a heat-flux term that describes anisotropic electron thermal conduction in a magnetic field and a term that describes electron-ion equilibration as follows

$$\frac{\partial \rho}{\partial t} + \nabla \cdot (\rho \mathbf{v}) = 0, \quad (1)$$

$$\frac{\partial \rho \mathbf{v}}{\partial t} + \nabla \cdot \left(\rho \mathbf{v} \mathbf{v} - \frac{\mathbf{B} \mathbf{B}}{4\pi} \right) + \nabla p = 0, \quad (2)$$

$$\frac{\partial E}{\partial t} + \nabla \cdot \left[\mathbf{v}(E + p) - \frac{\mathbf{B}(\mathbf{v} \cdot \mathbf{B})}{4\pi} \right] = -\nabla \cdot \mathbf{Q}, \quad (3)$$

$$\frac{\partial \mathbf{B}}{\partial t} + \nabla \cdot (\mathbf{B} \mathbf{v} - \mathbf{v} \mathbf{B}) = 0, \quad (4)$$

$$\frac{\partial s_e}{\partial t} + \nabla \cdot (s_e \mathbf{v}) = \left[\frac{ds_e}{dt} \right]_{ei} + \left[\frac{ds_e}{dt} \right]_{ee}, \quad (5)$$

where

$$p = p_i + p_e + \frac{B^2}{8\pi}, \quad (6)$$

$$E = \frac{\rho v^2}{2} + \frac{p_i + p_e}{\gamma - 1} + \frac{B^2}{8\pi}, \quad (7)$$

$$s_e = \rho \log(p_e / \rho^\gamma), \quad (8)$$

$$\mathbf{Q} = -\kappa_{\parallel} \mathbf{b} \mathbf{b} : \nabla T_e, \quad (9)$$

where ρ is the mass density (taken to be the ion mass density), \mathbf{v} the fluid velocity (assumed same for both species), p_i and p_e are the ion and electron pressures, \mathbf{B} the magnetic field, s_e the electron entropy, and \mathbf{Q} the heat flux along the magnetic field lines whose direction is set by unit vectors \mathbf{b} . Both electron and ion components are described by an ideal equation of state $p_{e/i} = n_{e/i} T_{e/i}$ (temperature is in energy units), where $n_e = n_i = \rho / m_i$ are the particle number densities (equal by plasma quasineutrality), and adiabatic index $\gamma = 5/3$. For the parallel thermal conductivity, we use the Spitzer value (Spitzer & Härm 1953) $\kappa_{\parallel} \approx 0.9 n_e \lambda_e v_{\text{the}}$, where n_e is the electron density, $v_{\text{the}} = (2T_e / m_e)^{1/2}$ is the electron thermal speed, and

$$\lambda_e \approx 0.1 \text{ kpc} \left(\frac{T_e}{4 \text{ keV}} \right)^2 \left(\frac{n_e}{4 \times 10^{-2} \text{ cm}^{-3}} \right)^{-1} \quad (10)$$

is the Coulomb electron mean free path in a hydrogen plasma expressed using characteristic parameters of the Perseus core in the vicinity of the observed weak shock. The two terms on the right-hand side of equation (5) describe dissipation due to electron-ion and electron-electron collisions.

Numerically, the dissipation terms are treated separately at the end of each time (sub-)step. First, the system of conservation laws for $(\rho, \rho \mathbf{v}, \mathbf{B}, E, s_e)$ described by equations (1)–(5) with the RHS set to zero is evolved by a second-order van Leer integrator using the HLLD flux (Miyoshi & Kusano 2005) modified to include electron pressure. The magnetic field is integrated via the constrained transport technique (Stone & Gardiner 2009). Second, electron thermal conduction is added by solving anisotropic heat transfer equation

$$\frac{\rho}{(\gamma - 1)m_i} \frac{\partial T_e}{\partial t} = -\nabla \cdot \mathbf{Q} \quad (11)$$

using Runge-Kutta-Legendre super-time-stepping (Meyer et al. 2012, 2014) with a monotonized central limiter applied to transverse temperature gradients to avoid temperature oscillations (Sharma & Hammett 2007, 2011). Finally, electron-ion equilibration is accounted for

by implicit integration (this might be a numerically stiff problem when the equilibration is fast) of equation

$$\frac{\partial(T_e - T_i)}{\partial t} = -\nu_{ei}(T_e - T_i), \quad (12)$$

where

$$\begin{aligned} \nu_{ei} &\approx 4 \frac{m_e v_{the}}{m_p \lambda_e} \\ &\approx 5 \times 10^{-16} \text{ s}^{-1} \left(\frac{T_e}{4 \text{ keV}} \right)^{-3/2} \left(\frac{n_e}{4 \times 10^{-2} \text{ cm}^{-3}} \right) \end{aligned} \quad (13)$$

is the thermal equilibration rate (Book 1983). The new electron temperature is then used to update the electron entropy s_e (which corresponds to adding the two dissipative terms on the RHS of equation 5) and total energy density E (only due to thermal conduction).

We also perform a series of single-fluid hydrodynamic runs with or without thermal conduction, where the same system of equations is solved with $p = 2p_i = 2p_e = 2n_e T_e$ excluding the induction equation (4) and equation (5) for the electron entropy, as well as runs with isotropic thermal conduction, where instead of equation (9), the heat flux is $Q = -\kappa_{\parallel} \nabla T_e$.

2.2 Numerical setup

As we are not concerned about the distribution of energy released during an AGN outburst between the radio bubble and the weak shock, it is sufficient to produce a spherical blast wave by the simplest suitable initial condition. The only requirement is that the shock needs to have Mach number $M \approx 1.2$ as it reaches radius $r \approx 15$ kpc to match observations of the weak shock in the Perseus cluster. Therefore, for the initial conditions, we produce an overpressurized (by a factor of ~ 100) region within $r < 1.5$ kpc, large enough to avoid pixelation. The weak shock produced in the outburst travels outward unimpeded, while the hot gas shell formed at the center is of no relevance for our problem. Following the outburst, we observe how the shock is modified by thermal conduction and electron-ion equilibration as it propagates to $r = 15$ kpc. Our 3D numerical box has size $L = 40$ kpc and is centered around the shock. We choose to use Cartesian coordinates because of the easier implementation of runs with tangled magnetic fields.

The observed part of the spherical weak shock in the Perseus cluster is located ≈ 25 kpc away from the cluster center in the north-east direction (its geometrical center is ≈ 10 kpc off the cluster center). In the vicinity of the shock, the ICM has temperature $T_0 \approx 4$ KeV and the radial temperature profile is flat (e.g., Graham et al. 2008; Zhuravleva et al. 2015). The ICM density in this region is $n_0 \approx 0.04 \text{ cm}^{-3}$. In our simulations, we choose to use uniform background temperature and density for several reasons. First, both radial profiles within the shock sphere are relatively flat (e.g., Zhuravleva et al. 2015). Second, there exists uncertainty about the initial density and temperature distribution at the moment of the AGN outburst that launched the shock, and it is likely that the initial distribution was different from the one currently observed. More importantly for our particular problem, the structures we are interested in, i.e., distortions of the shock due to thermal conduction, develop quickly (compared to the time it

takes for the shock to reach its current position) and locally, within ~ 5 kpc from the shock front. Therefore, it is sufficient to initialize the background density and temperature to those currently observed near the shock, as long as the simulated shock has the right Mach number $M \approx 1.2$ at radius $r \approx 15$ kpc.

There is currently a lot of uncertainty about the structure of magnetic field in the ICM, mainly due to the complicated physics of turbulent magnetized plasmas at high ratios of thermal to magnetic pressures and, on the other hand, limited possibilities to infer a 3D spectrum of magnetic fluctuations from radio observations (e.g., Carilli & Taylor 2002; Govoni & Feretti 2004; Feretti et al. 2012; Vogt & Enßlin 2005; Bonafede et al. 2010; Kuchar & Enßlin 2011). The magnetic spectrum is likely anisotropic, meaning the length scale of change of the field along itself is different (normally larger) than that transverse to itself (e.g., Schekochihin & Cowley 2006). The parallel correlation length is expected to be set by large-scale hydrodynamic motions (on those scales the field is too weak to have any dynamic effect on the fluid). But the perpendicular correlation scale depends on the intricacies of plasma turbulence and ranges from Larmor to injection scales depending on the numerical experiment and its interpretation (for MHD/Braginskii turbulence, see Haugen et al. 2004; Schekochihin et al. 2004; Maron et al. 2004; Cho & Ryu 2009; Beresnyak & Lazarian 2009; Beresnyak 2012; Santos-Lima et al. 2014; St-Onge et al. 2020; for kinetic turbulence, see Rincon et al. 2016; St-Onge & Kunz 2018). Rotation measure (meaning rotation of the polarization plane of synchrotron radiation as it travels through a magnetic field) observations of some clusters and groups of galaxies give estimates of the perpendicular scale of order several kpc (Vogt & Enßlin 2005; Bonafede et al. 2010; Kuchar & Enßlin 2011). In any case, for the problem of anisotropic thermal conduction in a static (on time scales of shock propagation) tangled magnetic field, the more relevant correlation length is parallel. This is because heat diffusion is not affected by field reversals: diffusion operates in layers of antiparallel field lines the same way as in a uniform field. Then for qualitative purposes, it is sufficient to use a statistically isotropic field on scales characteristic of gas motions induced by AGN activity or gas sloshing in the Perseus cluster. These scales likely range from a few to several tens kpc corresponding to the size of structures (radio bubbles, filaments, sloshing-induced spiral patterns) seen in *Chandra* X-ray images (Fabian et al. 2006). For this reason, we model the magnetic field simply as a random isotropic solenoidal 3D field with coherence length $l_B \approx 10$ kpc. The field is set to be very weak, so it does not have a dynamic feedback on the plasma. Such coherence length is somewhat larger than the width of conductive weak shocks in our simulations (~ 5 kpc).

Thermal conduction along the magnetic field lines operates via heat flux (9) with electron mean free path (10). To reduce the unnecessary computational load, we turn off thermal conduction in the central 6-kpc region that quickly becomes dominated by the hot shell. Initially, the ion and electron temperatures are set equal.

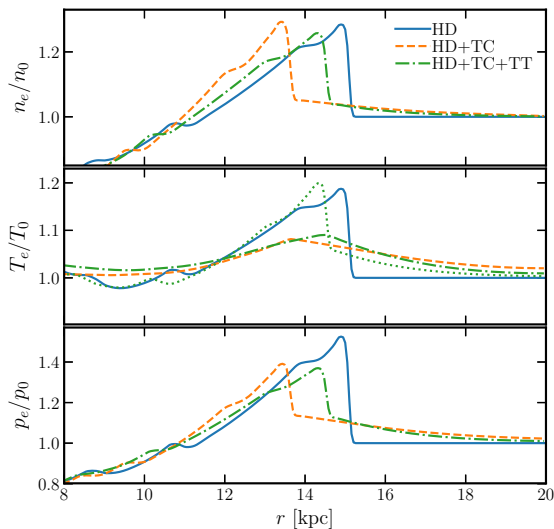


Figure 1. Profiles of electron density (upper panel), temperature (middle panel), and pressure (lower panel) in 3 different models: single-temperature hydrodynamics without (solid line) and with (dashed) thermal conduction and two-temperature hydrodynamics with conduction (dash-dotted). The dotted line shows the ion temperature in the third model. Both profiles are normalized to the pre-shock values. The x -axis shows the distance from the center of the outburst.

3 RESULTS

3.1 Isotropic thermal conduction

First, we analyze 1D hydrodynamic runs with a thermal conductivity at full Spitzer level. This models a configuration in which the magnetic field is radial and does not impede conduction. Fig. 1 shows the effects of thermal conduction and a finite electron-ion equilibration time relative to pure single-fluid hydrodynamics. In pure hydrodynamics (solid line), the density and temperature jumps agree with the Rankine-Hugoniot relations for a shock with Mach number $M \approx 1.18$:

$$\frac{n_2}{n_1} = \frac{\gamma + 1}{\gamma - 1 + 2/M^2} \approx 1.27, \quad (14)$$

$$\frac{T_2}{T_1} = \frac{(2\gamma M^2 - (\gamma - 1))((\gamma - 1)M^2 + 2)}{(\gamma + 1)^2 M^2} \approx 1.18. \quad (15)$$

Activating thermal conduction leads to formation of a temperature and, to a lesser extent, pressure and density precursors (dashed line in Fig. 1). Its length is consistent with the simple estimate of the distance l_{diff} that the electrons are able to diffuse in front of the shock based on equating the diffusion time and the time it takes for the shock to travel the diffusion length. The former is $t_{\text{diff}} \sim l_{\text{diff}}^2 / (\lambda_e v_{\text{the}})$, the latter $t_{\text{sh}} \sim l_{\text{diff}} / (M v_{\text{thi}})$. Then $l_{\text{diff}} \sim (m_i/m_e)^{1/2} \lambda_e$. Recalling that $\lambda_e \approx 0.1$ kpc (equation 10), we get $l_{\text{diff}} \sim 4$ kpc, in agreement with Fig. 1. In comparison with ideal hydrodynamics, the temperature jump becomes smaller due to thermal conduction, and because the gas becomes closer to isothermal, the shock starts to slightly lag behind.

Enabling different temperatures (dash-dotted line in Fig. 1) for the electrons and ions leads to little changes of the electron temperature profile, but the density profile be-

comes much closer to the hydrodynamic case. This happens because the electrons diffusing ahead of the shock do not have sufficient time to heat the ions (the ion temperature is shown in the lower panel of Fig. 1 by the dotted line). Because now the ions are mostly adiabatic, the speed of sound rises relative to the model with instant equilibration, and, therefore, the shock lags less.

Our single-temperature models produce weak shock profiles qualitatively similar to Graham et al. (2008) (see their Fig. 7; note that we do not match the shock front locations for different models in Fig. 1). Even though these authors use a more elaborate model of the outburst and introduce a smooth background density gradient, the weak shock itself is not sensitive to the initial conditions, and its profile is mainly determined by the intensity of thermal conduction across the shock. Our two-temperature model, however, is significantly different. While Graham et al. (2008) approximate the decoupling of electrons and ions by doubling the effective thermal conductivity, we solve a separate equation for the electron temperature, which is coupled to the ion temperature by a collision operator. This leads to noticeably different density and temperature profiles: namely, the ions tend to preserve their density and temperature jumps much better compared to the single-fluid model with conduction, while the electron temperature behaves the same as the gas temperature in the single-fluid model (compare this with the blue dotted line in Fig. 7 of Graham et al. 2008).

We can use the simulated density and temperature profiles in combination with large-scale radial profiles observed in the Perseus cluster to produce mock surface brightness maps and compare them with X-ray observations of the weak shock in the Perseus cluster. Given its spatial resolution, the most appropriate comparison data are from the *Chandra* Advanced Camera for Imaging Spectroscopy (ACIS). We obtained all ACIS observations of the core of Perseus that did not employ the diffraction gratings, totalling 900ks of good data spread across 21 separate observations (ObsIDs). Each of separate ObsIDs were reprocessed up to the calibration version 4.8.1 using CIAOv4.10, and then were merged into a single events file from which we extract a 0.7–4keV band image. We analyze a 40×40 kpc region of the Perseus core that contains the weak shock. The final image, shown in Fig. 2, has been divided by an appropriate β -model with central density $n_c = 0.05 \text{ cm}^{-3}$, core radius $r_c = 29$ kpc, and $\beta = 0.53$ (Zhuravleva et al. 2015) and smoothed with a Gaussian filter of size $\sigma \approx 1'' \approx 0.4$ kpc. Its bottom right corner coincides with the geometrical center of the shock sphere. In our energy range, the emissivity of an optically thin plasma is almost independent of temperature observed by the ACIS-S detector on *Chandra* (e.g., Forman et al. 2007; Zhuravleva et al. 2015). Therefore, surface brightness is simply an integral of the electron density squared along the line of sight.

In order to model the observed scaled X-ray surface brightness by integrating the emissivity along the line of sight, we need to know the large-scale ICM density distribution. In our simulations, we have used a uniform density and temperature background (see Section 2.2). This is justified because the β -model in the vicinity of the shock (its width including the precursor is $\lesssim 10$ kpc) is smooth. Then we can factorize the large-scale electron density as $n_e(x, y, z) = n_{e0}(r) \times n_{e,\text{sim}}(r_s)$, where $n_{e0}(r) = n_c [1 + (r/r_c)^2]^{-3/2\beta}$ is

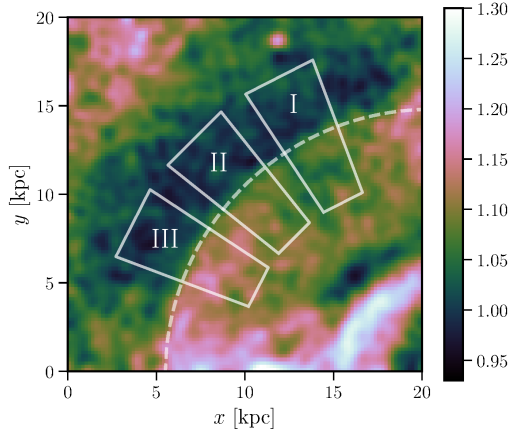


Figure 2. A *Chandra* X-ray image of the weak shock ≈ 10 kpc north-east of the center of the Perseus cluster. The image shows the X-ray surface brightness divided by a smooth β -model with parameters $\beta = 0.53$ and $r_c = 29$ kpc and convolved with a Gaussian filter of size $\sigma \approx 1'' \approx 0.4$ kpc. The surface brightness is normalized to its average value in the pre-shock region. The superimposed sectors are the areas used to produce surface brightness profiles in Fig. 3.

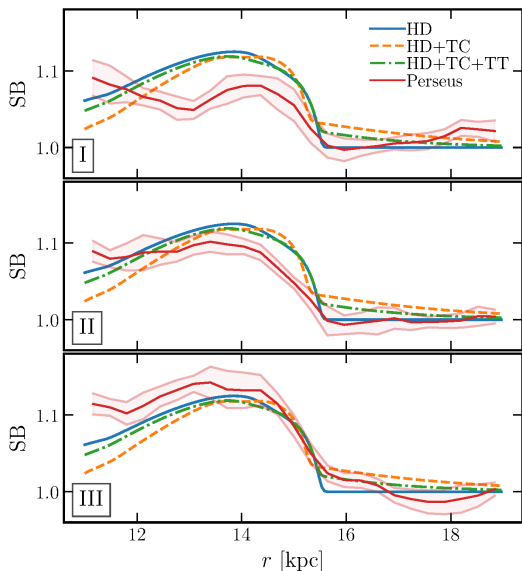


Figure 3. Surface brightness profiles calculated from the 1D simulations (same as in Fig. 1) using equation (16) compared with those extracted from the Perseus X-ray image in Fig. 2) (red lines). The surface brightness is normalized to the pre-shock region. The x -axis is the distance from the geometrical center of the shock sphere. The error bars indicate the rms fluctuations of surface brightness in the 25 bins used for averaging over the sectors in Fig. 2. The shock locations in the different runs have been matched to facilitate the comparison.

the smooth background β -model and $n_{e,\text{sim}}(r_s)$ is the simulated electron density (shown in the upper panel of Fig. 1). The former is a function of the distance from the center of the cluster $r = (x^2 + y^2 + z^2)^{1/2}$, where x, y are the sky coordinates relative to the cluster center and z is the distance along the line of sight. The latter is a function of the distance from the center of the shock sphere (x_{0s}, y_{0s}):

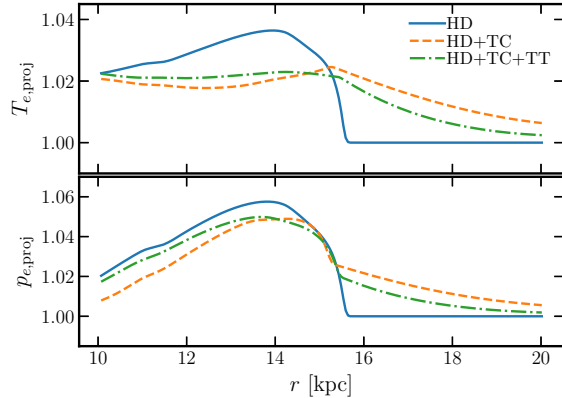


Figure 4. Projected temperature (upper panel) and electron pressure (lower panel) profiles calculated from the 1D runs (same as in Fig. 1) using equation (17) and equation (19). Both quantities are normalized to the pre-shock values. The shock locations in the different runs have been matched.

$r_s = ((x - x_{0s})^2 + (y - y_{0s})^2 + z^2)^{1/2}$. Then the mock surface brightness divided by the β -model is

$$\text{SB}(x, y) = \frac{\int_0^\infty [n_{e,\text{sim}}(x, y, z) \times n_{e0}(x, y, z)]^2 dz}{\int_0^\infty [n_{e0}(x, y, z)]^2 dz}. \quad (16)$$

In Fig. 2, the cluster center is located at $x \approx 26$ kpc, $y \approx -8$ kpc.

In Fig. 3, we compare the mock surface brightness profiles for the three 1D models of the weak shock with surface brightness profiles obtained from the X-ray data by averaging over the three different sectors in Fig. 2. The locations of the simulated shocks have been matched to facilitate the comparison. While it is rather difficult to distinguish between the pure hydrodynamic model and the one with both thermal conduction and ion-electron equilibration enabled, we see no indication of a conductive precursor, except for the third region, where variations of surface brightness before the shock preclude simple assessment. Deviations of the electron density from the β -model manifested in the significant variation of the observed profiles in the three chosen regions, particularly in the upstream region where precursors could be produced, also make further matching with our models problematic.

In addition, we can calculate the projected electron temperature $T_{e,\text{proj}}(x, y)$ using the simulated data $T_{e,\text{sim}}(r_s)$ (shown in the lower panel of Fig. 4) by weighting the temperature with the emissivity and dividing it by the smooth background as follows

$$T_{e,\text{proj}} = \frac{\int_0^\infty (T_{e,\text{sim}} \times T_{e0})(n_{e,\text{sim}} \times n_{e0})^2 dz}{\int_0^\infty (n_{e,\text{sim}} \times n_{e0})^2 dz} \times \left[\frac{\int_0^\infty T_{e0} n_{e0}^2 dz}{\int_0^\infty n_{e0}^2 dz} \right]^{-1}, \quad (17)$$

where

$$T_{e0} = T_{ec} \frac{1. + (r/r_c)^{3.5}}{1 + 0.4(r/r_c)^{3.6}} \quad (18)$$

is the background temperature profile with $T_{ec} = 4$ keV and $r_c = 58$ kpc taken from Zhuravleva et al. (2015). We have omitted the coordinate (x, y, z) -dependence in equation (17)

for brevity. We have factorized the large-scale temperature analogously to the density. The projected temperature profiles as functions of the distance from the center of the outburst are demonstrated in the upper panel of Fig. 4. Both models with thermal conduction lead to formation of a ~ 4 -kpc long temperature precursor, and the difference between these models and the hydrodynamic model is much more prominent than that seen in the surface brightness maps.

Finally, it is possible to measure variations of electron pressure in cluster cores by employing the Sunyaev-Zeldovich (SZ) effect (Sunyaev & Zeldovich 1972), which manifests itself as distortions of the cosmic microwave background (CMB) radiation in the direction of galaxy clusters due to Compton scattering of the CMB photons off the hot ICM electrons. The magnitude of the SZ effect is proportional to the integral of electron pressure along the line of sight. Therefore, we can produce the SZ map divided by the background model from our simulations:

$$p_{e,\text{proj}}(x, y) = \frac{\int_0^\infty (n_{e,\text{sim}} T_{e,\text{sim}}) \times (n_{e0} T_{e0}) dz}{\int_0^\infty n_{e0} T_{e0} dz}. \quad (19)$$

The result is shown in the lower panel of Fig. 4: as one may have expected, the conductive precursor is now less prominent than in the projected temperature, but stronger than in the surface brightness profiles.

3.2 Anisotropic thermal conduction

Let us now switch to the 3D runs with anisotropic thermal conduction. For these simulations, we initialize a weak random isotropic magnetic field with coherence length $l_B \approx 10$ kpc (as justified in Section 2.2). Anisotropic conduction imprints the characteristic correlation scale of the magnetic field onto the density and temperature structure of the shock front, as seen clearly in Fig. 5. When ion-electron equilibration is instant, both temperature and density jumps of the shock become distorted. The distortion is caused by two effects. First, the jumps are smoothed in regions where the magnetic field is largely radial, while they stay sharper where the field is close to tangential. Second, the shock front becomes corrugated because strong thermal conduction along radial field lines reduces the temperature jump (as seen in Fig. 1 for the 1D models), the shock becomes more isothermal and slows down, while if the field is tangential, it propagates at the adiabatic speed of sound as in ideal hydrodynamics. A finite temperature equilibration time attenuates the link between the ions and electrons, allowing the former to retain the sharpness of the density jump. The shock front is also less corrugated because the ions now preserve their temperature jump. The electron temperature map, however, stays qualitatively unchanged.

We now use the 3D runs to produce surface brightness maps using the same approach as before (equation 16). The results are demonstrated in Fig. 6. The model with instant ion-electron equilibration expectedly leads to noticeable distortions of the shock front, even though projection effects blur the density variations seen more prominently in Fig. 5. Introducing gradual ion-electron equilibration yields a surface brightness map hardly distinguishable from pure hydrodynamics. The current Perseus data (right panel of Fig. 6) does not allow one to distinguish between the two models.

Analogously, we obtain projected temperature maps by

applying equation 17 to the 3D simulated temperature. The result can be seen in the upper row of Fig. 7. Distortions of the shock front are now seen in both models because electron temperature is relatively unaffected by a finite equilibration time. The maps of electron pressure integrated along the line of sight are demonstrated in the lower row of Fig. 7.

The above results stay qualitatively the same as long as the coherence length of the magnetic field is appreciably larger than the shock width (~ 5 kpc). If the field is tangled on smaller scales (which, however, appears unlikely because the field is naturally expected to be produced by turbulent gas motions driven by the jet-bubble dynamics on scales ~ 10 kpc), the distortions of the shock front associated with the topology of the field become averaged out (even more so by the projection effects). In this case, one can introduce an effective isotropic thermal conductivity as a fraction of the Spitzer value determined by the statistics of the field lines. Due to the current lack of the complete theory of high- β MHD turbulence, the exact value of such effective conductivity cannot be calculated. One way to provide its estimate is to apply the theory of strong MHD turbulence, based on the assumption of the so-called critical balance (Goldreich & Sridhar 1995), locally to calculate how quickly magnetic field lines diverge and, thus, how quickly thermal electrons spread in space (Narayan & Medvedev 2001). Such calculation leads to effective conductivities of order $1/5$ – $1/3$ of the Spitzer value. Then, the case of small-scale magnetic fields is simply reduced to a 1D model with a smaller conductivity. The opposite case of a very large-scale magnetic field on scales of tens of kpc is trivial and described by the 1D model at full Spitzer conductivity along the direction of the field, and ideal hydrodynamics (assuming the field is weak) in the perpendicular plane.

4 DISCUSSION

4.1 Relevance for present and future observations

The 900 ks *Chandra*/ACIS imaging spectroscopy of weak shocks in the core of the Perseus cluster currently give us our best view of bulk transport properties on scales approaching the electron mean-free-path. Even this dataset, however, is not able to provide tight constraints on the presence or absence of conductive precursors once finite electron-ion equilibration is taken into account. Significantly deeper *Chandra*/ACIS observations (bringing the core exposure to ~ 3 Ms) would permit sufficiently accurate measurements of (projected) temperature profiles across the shock to address suppression of electron thermal conduction parallel to the magnetic field, providing an important complement to existing limits on perpendicular heat transport at cold fronts.

The equilibration issue can be sidestepped in our study of electron heat transport if we are able to measure electron and ion temperatures separately. This requires high-spectral resolution so that the (electron) bremsstrahlung can be cleanly separated from the ionic emission lines, and it requires high signal-to-noise so that the ion temperature can be determined from the ratio of charge states of given elements. With only modest spectral resolution ($E/\Delta E \sim 100$), *Chandra*/ACIS is unable to conduct such a study. Separate measurements of T_e and T_i were performed

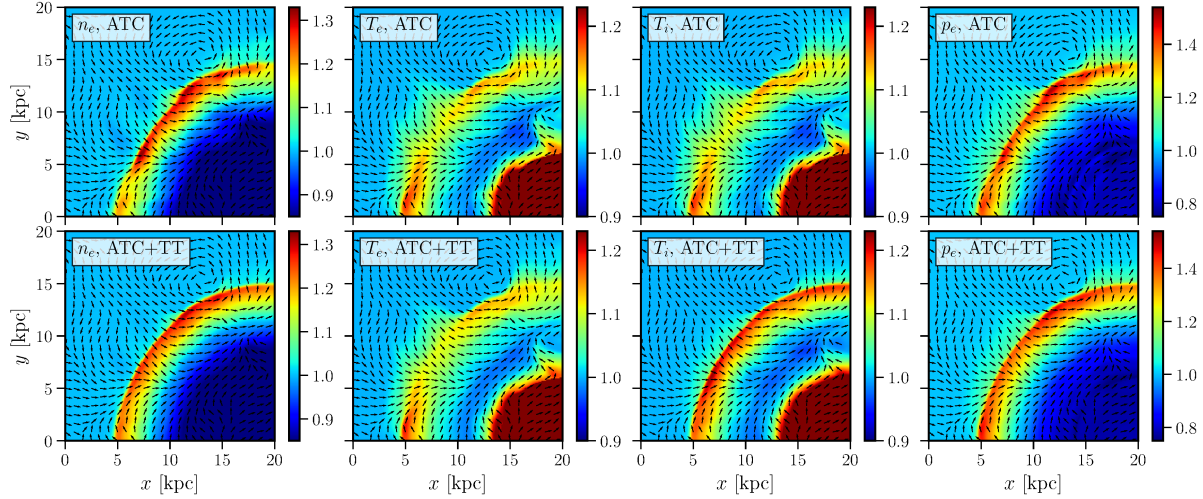


Figure 5. Midplane ($z=0$) 3D slices of the electron density (left column), electron temperature (second from left), ion temperature (second from right), and electron pressure (right) for the model with thermal conduction only (upper row) and both conduction and ion-electron temperature equilibration (lower row). All the quantities are normalized to the pre-shock values. The magnetic-field vectors are superimposed.

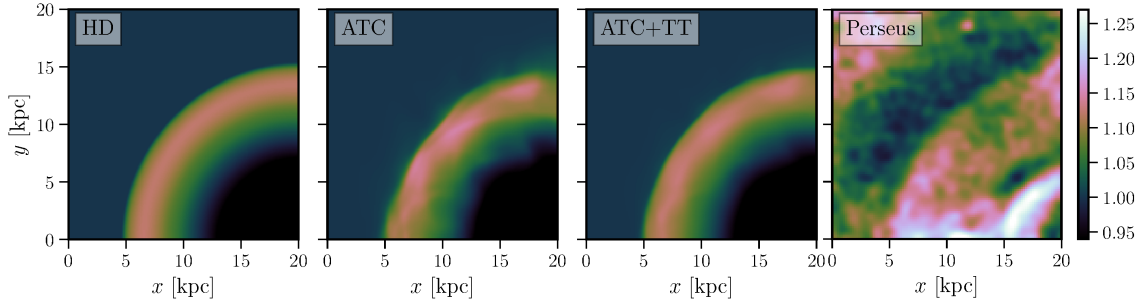


Figure 6. The mock surface brightness maps generated from the 3D simulations of weak shocks using equation (16) (the models are the same as in Fig. 5 with the addition of pure hydrodynamics in the left panel) compared with a *Chandra* X-ray image of the weak shock in the Perseus cluster (same as in Fig. 2). The images are normalized to the surface brightness in the pre-shock region.

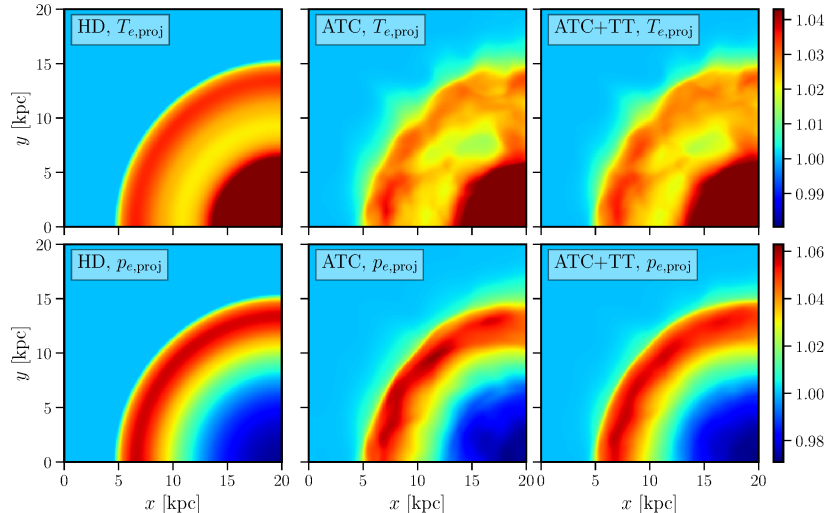


Figure 7. Projected temperature and pressure maps calculated from the 3D runs for the same models as in Fig. 6. Both quantities are normalized to the pre-shock region.

in the Perseus cluster by the micro-calorimeter on *Hitomi* satellite (Hitomi Collaboration et al. 2018), but the limited spatial resolution of these measurements meant that the spectrum encompassed essentially the entire inner core of the cluster. However, ATHENA (c2031, Barret et al. 2020) and *Lynx* (c2040, The Lynx Team 2018) will enable spatially resolved microcalorimeter resolution ($E/\Delta E \sim 1000$) spectroscopy, allowing us to map T_e and T_i separately. *Lynx*, with its subarcsecond spatial resolution, will be a particularly powerful observatory for probing the physics of transport on mean-free-path scales in ICM plasmas.

4.2 Applicability to weak shocks in clusters other than Perseus

In our study, we have used the weak shock in the Perseus cluster as a fiducial model. We have done so for several reasons. First, the shock appears remarkably regular, without any significant distortions of the front, which allows one to put constraints on processes that can potentially deform the shock. Second, the *Chandra* X-ray observatory has provided a wealth of high-resolution data for the Perseus core, allowing us to limit the shock width down to ~ 1 kpc. Finally, because the shock is very weak ($M \sim 1.2$), nonlinear kinetic effects could be subdominant (but see Section 4.3), and it should be approximated by fluid models better. However, there is at least one more example of a prominent weak shock in a cluster cool core: the shock in the giant elliptical galaxy M87, located ≈ 13 kpc from the cluster center, exhibits very similar qualities (regularity, low Mach number, and even the electron mean free path ~ 0.1 kpc), however the signal-to-noise ratio of its observations by *Chandra* is significantly lower than for Perseus. All our results should apply to M87, as well as any very weak shock in cluster cores where the electron mean free path is such that the size of the potential conductive precursor (~ 40 mean free paths) is significant to distinguish between the different models.

4.3 Collisional vs. collisionless shocks

We have studied the propagation of a weak shock with Mach number $M \sim 1.2$ in the ICM in a number of fluid models. In the Perseus cluster, the electron mean free path in the vicinity of the shock is ~ 0.1 kpc, which is 4 times smaller than the resolution of *Chandra*. Therefore we cannot infer from the data whether the shock is collisional or collisionless. Nevertheless, there are several *Chandra* observations of merger shocks at higher Mach numbers $M \sim 2-3$ on cluster outskirts where the mean free path reaches ~ 20 kpc. These observations indicate the presence of collisionless processes at play: e.g., Markevitch (2006) argued that the electron-ion equilibration time at the shock in the Bullet cluster is much shorter than the Spitzer value, while Russell et al. (2012) were able to measure the width of one of the two shocks in Abell 2146 at ~ 6 kpc, roughly 4 times smaller than the Coulomb mean free path.

Let us discuss the latter observation first. We note that even if the shock is collisionless, i.e., there is ion scattering by plasma instabilities that generates entropy at the shock, the electrons might still be able to transfer heat across the shock, even though they are compressed with the ions by the

electric fields ensuring plasma quasineutrality, unless electron plasma instabilities develop as well. In this case, when the heat flux is still mediated by Coulomb interactions, a conductive precursor can develop in the upstream region identically to our simulations. However, this may not be the case, at least for higher Mach number $M \sim 2-3$ shocks, as we speculate below.

Markevitch (2006) showed that the electron temperature behind the shock in the Bullet cluster quickly becomes close to the ion post-shock temperature, suggesting the presence of a kinetic mechanism that heats the electrons above the adiabatic compression. Di Mascolo et al. (2019), however, used observations of the SZ effect by the Atacama Large Millimeter/submillimeter Array and Atacama Compact Array to argue that collisional electron-ion equilibration leads to a better agreement between the radio and *Chandra* X-ray data. A general discussion on the electron-ion temperature ratio at collisionless shocks can be found in Vink et al. (2015). Fundamentally, this process needs to be studied by means of particle-in-cell plasma simulations. However, the regime of low Mach numbers and high plasma beta relevant for the ICM was investigated only recently (Guo et al. 2014a,b, 2017, 2018; Ha et al. 2018; Kang et al. 2019). In particular, Guo et al. (2017) proposed a mechanism for electron heating at quasi-perpendicular shocks via betatron acceleration of electrons by the amplified magnetic fields (both due to the shock itself and the associated ion instabilities in the downstream region) combined with scattering by electron whistler waves that disrupts the conservation of electron magnetic moment, thermalizes particles, and generates entropy. For our problem, the heating itself is irrelevant, because for very weak shocks the difference between the shock and adiabatic heating is small. On the other hand, the potential generation of whistlers at the shock is important, because even for small shock compression ratios of ~ 1.3 the electron temperature anisotropy generated by the amplified field via adiabatic invariance may exceed the whistler instability threshold:

$$\frac{T_{\perp}}{T_{\parallel}} - 1 \approx \frac{0.21}{\beta_{\parallel}^{0.6}}, \quad (20)$$

where T_{\perp} and T_{\parallel} are the perpendicular and parallel (to the local magnetic field) temperatures, and β_{\parallel} is the ratio of the parallel electron pressure to the magnetic-energy density (Gary et al. 2005). From adiabatic invariance, the temperature ratio is roughly the amplification factor of the magnetic field (equal to the shock compression ratio), which is ~ 1.3 for Mach number $M \sim 1.2$, so the left-hand side of equation (20) is ~ 0.3 . The electron plasma beta in cluster cores is typically ~ 100 , which gives the right-hand side of equation (20) ~ 0.01 . We see that the instability threshold is clearly exceeded even for very weak shocks. In case the whistlers are indeed important, our results can be reformulated as follows: if no precursors or deformations of the shock are observed, this could be a signature of electron scattering by whistler waves at the shock.

5 CONCLUSION

In this work, we have studied different models of propagation of a very weak shock in the ICM, using the weak shock

with $M \approx 1.2$ observed in the core of the Perseus cluster as a fiducial model. Compared to ideal hydrodynamics, introducing isotropic thermal conduction at full Spitzer value leads to formation of a conductive precursor with length of order 40 electron mean free paths (~ 4 kpc) and a decrease of the temperature jump at the shock. When the thermal link between the electrons and ions is reduced by a finite equilibration time, the density precursor is significantly suppressed, while the electron temperature profile stays roughly the same. There is no conclusive evidence of a precursor in the X-ray images of the Perseus weak shock we have analyzed.

Anisotropic thermal conduction across the weak shock produces temperature and density distortions along the shock that are coherent with the structure of the magnetic field, mainly its parallel correlation length. The electron temperature distortions are preserved almost intact in the two-temperature model, while the density variations are largely wiped out and appear close to ideal hydrodynamics.

ACKNOWLEDGEMENTS

C.S.R. thanks the UK Science and Technology Facilities Council (STFC) for support under the New Applicant grant ST/R000867/1, and the European Research Council (ERC) for support under the European Unions Horizon 2020 research and innovation programme (grant 834203). EC acknowledges support by the Russian Science Foundation grant 19-12-00369.

REFERENCES

- Barret D., Decourchelle A., Fabian A., Guainazzi M., Nandra K., Smith R., den Herder J.-W., 2020, *Astron. Nachr.*, 341, 224
- Beresnyak A., 2012, *Phys. Rev. Lett.*, 108, 035002
- Beresnyak A., Lazarian A., 2009, *ApJ*, 702, 1190
- Bonafede A., Feretti L., Murgia M., Govoni F., Giovannini G., Dallacasa D., Dolag K., Taylor G. B., 2010, *A&A*, 513, A30
- Book D. L., , 1983, *NRL (Naval Research Laboratory) plasma formulary*, revised, Naval Research Lab. Report
- Carilli C. L., Taylor G. B., 2002, *A&A*, 40, 319
- Cho J., Ryu D., 2009, *ApJ*, 705, L90
- Churazov E., Forman W., Jones C., Böhringer H., 2000, *A&A*, 356, 788
- Dennis T. J., Chandran B. D. G., 2005, *ApJ*, 622, 205
- Di Mascolo L., Mroczkowski T., Churazov E., Markevitch M., Basu K., Clarke T. E., Devlin M., Mason B. S., Randall S. W., Reese E. D., Sunyaev R., Wik D. R., 2019, *A&A*, 628, A100
- Fabian A. C., 2012, *ARA&A*, 50, 455
- Fabian A. C., Reynolds C. S., Taylor G. B., Dunn R. J. H., 2005, *MNRAS*, 363, 891
- Fabian A. C., Sanders J. S., Taylor G. B., Allen S. W., Crawford C. S., Johnstone R. M., Iwasawa K., 2006, *MNRAS*, 366, 417
- Fabian A. C., Walker S. A., Russell H. R., Pinto C., Sanders J. S., Reynolds C. S., 2017, *MNRAS*, 464, L1
- Fang X.-E., Guo F., Yuan Y.-F., Mou G., 2018, *ApJ*, 863, 177
- Feretti L., Giovannini G., Govoni F., Murgia M., 2012, *A&A Rev.*, 20, 54
- Forman W., Churazov E., Jones C., Heinz S., Kraft R., Vikhlinin A., 2017, *ApJ*, 844, 122
- Forman W., Jones C., Churazov E., Markevitch M., Nulsen P., Vikhlinin A., Begelman M., Böhringer H., Eilek J., Heinz S., Kraft R., Owen F., Pahre M., 2007, *ApJ*, 665, 1057
- Fujita Y., Suzuki T. K., 2005, *ApJ*, 630, L1
- Gary S. P., Lavraud B., Thomsen M. F., Lefebvre B., Schwartz S. J., 2005, *Geophys. Res. Lett.*, 32, L13109
- Goldreich P., Sridhar S., 1995, *ApJ*, 438, 763
- Govoni F., Feretti L., 2004, *IJMPD*, 13, 1549
- Graham J., Fabian A. C., Sanders J. S., 2008, *MNRAS*, 386, 278
- Guo F., Oh S. P., 2008, *MNRAS*, 384, 251
- Guo X., Sironi L., Narayan R., 2014a, *ApJ*, 794, 153
- Guo X., Sironi L., Narayan R., 2014b, *ApJ*, 797, 47
- Guo X., Sironi L., Narayan R., 2017, *ApJ*, 851, 134
- Guo X., Sironi L., Narayan R., 2018, *ApJ*, 858, 95
- Ha J.-H., Ryu D., Kang H., van Marle A. J., 2018, *ApJ*, 864, 105
- Haugen N. E., Brandenburg A., Dobler W., 2004, *Phys. Rev. E*, 70, 016308
- Hitomi Collaboration Aharonian F., Akamatsu H., Akimoto F., Allen S. W., Angelini L., Audard M., Awaki H., Axelsson M., Bamba A., Bautz M. W., Blandford R., 2018, *PASJ*, 70, 11
- Kang H., Ryu D., Ha J.-H., 2019, *ApJ*, 876, 79
- Komarov S., Schekochihin A. A., Churazov E., Spitkovsky A., 2018, *J. Plasma Phys.*, 84, 905840305
- Komarov S. V., Churazov E. M., Kunz M. W., Schekochihin A. A., 2016, *MNRAS*, 460, 467
- Kuchar P., Enßlin T. A., 2011, *A&A*, 529, A13
- Markevitch M., 2006, in Wilson A., ed., *The X-ray Universe 2005 Vol. 604 of ESA Special Publication, Chandra Observation of the Most Interesting Cluster in the Universe*. p. 723
- Markevitch M., Mazzotta P., Vikhlinin A., Burke D., Butt Y., David L., Donnelly H., Forman W. R., Harris D., Kim D.-W., Virani S., Vrtilek J., 2003, *ApJ*, 586, L19
- Maron J., Cowley S., McWilliams J., 2004, *ApJ*, 603, 569
- Meyer C. D., Balsara D. S., Aslam T. D., 2012, *MNRAS*, 422, 2102
- Meyer C. D., Balsara D. S., Aslam T. D., 2014, *J. Comp. Phys.*, 257, 594
- Miyoshi T., Kusano K., 2005, *J. Comp. Phys.*, 208, 315
- Narayan R., Medvedev M. V., 2001, *ApJ*, 562, L129
- Reynolds C. S., Heinz S., Begelman M. C., 2002, *MNRAS*, 332, 271
- Rincon F., Califano F., Schekochihin A. A., Valentini F., 2016, *Proc. NAS*, 113, 3950
- Roßberg-Clark G. T., Drake J. F., Reynolds C. S., Swisdak M., 2016, *ApJ*, 830, L9
- Roßberg-Clark G. T., Drake J. F., Reynolds C. S., Swisdak M., 2018, *Phys. Rev. Lett.*, 120, 035101
- Russell H. R., McNamara B. R., Sanders J. S., Fabian A. C., Nulsen P. E. J., Canning R. E. A., Baum S. A., Donahue M., Edge A. C., King L. J., O’Dea C. P., 2012, *MNRAS*, 423, 236

- Ruszkowski M., Brüggem M., Begelman M. C., 2004, *ApJ*, 611, 158
- Santos-Lima R., de Gouveia Dal Pino E. M., Kowal G., Falceta-Gonçalves D., Lazarian A., Nakwacki M. S., 2014, *ApJ*, 781, 84
- Schekochihin A. A., Cowley S. C., 2006, *Phys. Plasmas*, 13, 056501
- Schekochihin A. A., Cowley S. C., Taylor S. F., Maron J. L., McWilliams J. C., 2004, *ApJ*, 612, 276
- Shabala S. S., Alexander P., 2009, *MNRAS*, 392, 1413
- Sharma P., Hammett G. W., 2007, *J. Comp. Phys.*, 227, 123
- Sharma P., Hammett G. W., 2011, *J. Comp. Phys.*, 230, 4899
- Spitzer L., Härm R., 1953, *Phys. Rev.*, 89, 977
- St-Onge D. A., Kunz M. W., 2018, *ApJ*, 863, L25
- St-Onge D. A., Kunz M. W., Squire J., Schekochihin A. A., 2020, arXiv e-prints, p. arXiv:2003.09760
- Sternberg A., Soker N., 2009, *MNRAS*, 395, 228
- Stone J. M., Gardiner T., 2009, *New A*, 14, 139
- Sunyaev R. A., Zeldovich Y. B., 1972, *CoASP*, 4, 173
- Tang X., Churazov E., 2018, *MNRAS*, 477, 3672
- The Lynx Team 2018, arXiv e-prints, p. arXiv:1809.09642
- Vink J., Broersen S., Bykov A., Gabici S., 2015, *A&A*, 579, A13
- Vogt C., Enßlin T. A., 2005, *A&A*, 434, 67
- Werner N., McNamara B. R., Churazov E., Scannapieco E., 2019, *Space Sci. Rev.*, 215, 5
- Zhuravleva I., Churazov E., Arévalo P., Schekochihin A. A., Allen S. W., Fabian A. C., Forman W. R., Sanders J. S., Simionescu A., Sunyaev R., Vikhlinin A., Werner N., 2015, *MNRAS*, 450, 4184
- Zhuravleva I., Churazov E., Arévalo P., Schekochihin A. A., Forman W. R., Allen S. W., Simionescu A., Sunyaev R., Vikhlinin A., Werner N., 2016, *MNRAS*, 458, 2902
- Zhuravleva I., Churazov E., Schekochihin A. A., Allen S. W., Arévalo P., Fabian A. C., Forman W. R., Sanders J. S., Simionescu A., Sunyaev R., Vikhlinin A., Werner N., 2014, *Nature*, 515, 85

DATA AVAILABILITY

The data underlying this article will be shared on reasonable request to the corresponding author.